Composites Part B 200 (2020) 108325

Contents lists available at ScienceDirect

Composites Part B

journal homepage: www.elsevier.com/locate/compositesb

A multiscale model for optimizing the flexural capacity of FRC structural elements

C.A. Nonato Da Silva [a], J. Ciambella [a,*], J.A.O. Barros [b], T.D. dos Santos Valente [c], I.G. Costa [c]

[a] Department of Structural and Geotechnical Engineering, Sapienza University of Rome, Italy
[b] Departamento de Engenharia Civil, University of Minho, ISISE, IB-S, Portugal
[c] Civitest - Pesquisa de Novos Materiais para a Engenharia Civil, Portugal

ARTICLE INFO

Keywords:
Hooked end steel fibres
SFRC
Cohesive interface
Multiscale modelling

ABSTRACT

In the present work, a multiscale model for fibre reinforced concrete (FRC) beams failing in bending is presented. At the microstructural level, the fibre is modelled as a one-dimensional continuum with axial, shear and bending deformability, with cohesive-like interfaces to simulate the interaction with the surrounding concrete. At the macroscopic level, the response of the beam is simulated by discretising the cross-section into layers and by enforcing the proper compatibility conditions between the layers. In the post-cracking stage, the tensile capacity is assured by the fracture energy of the concrete and the fibre resisting mechanisms simulated by the fibre pull-out constitutive laws determined at the microstructural level. The model can account for fibre distribution and orientation, controlled by the casting conditions and geometry of the mould. By using experimental data available from the open literature, it is proved that such an integrated approach is able to derive, by inverse analysis, the stress-crack width relationship of FRC, which is the fracture mode I information in the material nonlinear analysis of FRC structures with approaches based on the finite element method.

1. Introduction

Adding discrete (small) fibres to concrete as a slender constituent of reinforcing functionalities has been used to enhance the mechanical properties in many engineering applications including pavements [1], tunnels [2], Reinforced Concrete (RC) structural components [3], pedestrian bridges [4], elevated steel fibre reinforced concrete slabs [5] and modular prefabricated constructions [6]. Small fibres with different geometries and material properties have been used for the production of Fibre Reinforced Concrete (FRC) due to their ability of offering resistance to crack opening and sliding, resulting benefits in terms of the performance of structural elements at Serviceability and Ultimate Limit State conditions (SLS, ULS, respectively) [7,8]. Furthermore, the addition of fibres enhances the post-peak structural ductility and the energy absorption capacity [9–11]. In terms of material, steel fibres have been the most used in FRC and can be divided into two groups: smooth fibres and irregular shape fibres. The latter are used to significantly improve the pull-out behaviour thanks to a mechanical anchorage effect [12,13]. This type of fibres has the advantage of providing high stress transfer capacity between the faces of a crack for a relatively large interval of crack opening, therefore, when Steel Fibre Reinforced Concrete (SFRC) is appropriately designed, significant benefits can be obtained at SLS and ULS conditions [14,15]. Among the different type of irregular shape fibres available in the market, hooked end fibres, characterised by an hook at each end, have been the most employed.

The hooked end contribution to the pull-out mechanism depends mainly on the fibre tensile strength, the hook geometry and the strength of the surrounding cement-based matrix [12]. The accurate description of the reinforcement mechanism provided by the hook is crucial for designing the fibre and optimizing the effectiveness of the reinforcement system. To better understating the reinforcement mechanism, many researchers have performed pull-out tests of a single hooked end fibre [10,14,16–19] and have proposed analytical formulation for modelling the bond behaviour [12,20–24]. In all these contributions, the pull-out of hooked end fibres was modelled with a certain inclination towards the applied load for capturing the relative orientation between the crack plane and the fibre. The additional effects caused by the bending of the fibre at its exit point influence the peak force and can change the failure mode of the system, which can either be the complete debonding of the fibre or the fibre rupture. Furthermore, the spalling mechanism at fibre exit point, which was observed for a hook end fibre above a certain orientation toward the crack plane, was mostly neglected in all available

* Corresponding author.
E-mail address: jacopo.ciambella@uniroma1.it (J. Ciambella).

https://doi.org/10.1016/j.compositesb.2020.108325
Received 21 May 2020; Received in revised form 3 July 2020; Accepted 31 July 2020
Available online 5 August 2020

models. Indeed, experiments carried out in Ref. [18] confirmed that the force necessary to completely pull-out the fibre from the matrix increases with the inclination angle up to a certain limit, above which spalling mechanism become predominant. In addition, it was observed that up to a certain inclination, the work required to completely debond the inclined fibre from the matrix was higher than the one of an aligned fibre.

Within the broad literature of fibre-reinforced concrete materials, an integrated approach to predict the flexural capacity of FRC structural elements is introduced in this paper. This integrated approach was implemented in DoCroS software [25] for determining the moment-curvature or momentrotation relationship of a concrete cross section that can be reinforced by steel and/or fibre reinforced polymer bars. In DoCroS, a cross section is discretized in layers, and each layer can be formed by different materials with their own constitutive laws. The new features of the integrated approach herein proposed are inspired in the model proposed by Ref. [26], by explicitly considering the presence of the fibres crossing the cross section. The crack opening process is iteratively controlled by assuring force equilibrium at the section level, compatibility of deformations and respecting the constitutive laws of all the intervenient materials. Fibres are disposed in the cross section according to fibre orientation profile model proposed by Ref. [27]. A preliminary version of this integrated approach was developed by Ref. [28] for assessing, by inverse analysis, the fibre pullout constitutive laws. In the present paper, the potentialities of this approach are extended by providing the possibility of integrating fibre pullout constitutive laws for the adopted fibre orientation profile, obtained from the application of the microstructural model described in Section 2.

The fibre pullout constitutive law for each interval of the fibre orientation profile is predicted by using a one-dimensional model of a hooked end fibre resting on a cohesive like-interface. This model extends an approach recently proposed by the authors [29] for smooth fibres and takes into consideration the increased complexity introduced by the hooked end. The fibre is modelled as one-dimensional continuum resting on a cohesive-like interface and can account for an arbitrary orientation of the fibre toward the crack plane and for all the relevant effects registered in the pull-out response, which are mostly neglected in the available literature contributions, including: fibre bending, matrix damage and matrix spalling. The capabilities of this microstructural model will be tested against the experimental data on the pull-out of a single fibre carried out in ([12,17–19]). In particular, the constitutive parameter extracted from Ref. [12] will be used to simulate the flexural capacity of the beam tested in Ref. [30], in which the same type of fibres and concrete were used.

2. Microstructural model to predict the local bond behaviour

The simulation of the effect of the hooked end on the pull-out response of a single fibre is the central task in this section. For this purpose, an extension of the analytical formulation recently introduced in Ref. [29] is here proposed in order to simulate the resisting mechanisms provided by a hooked end fibre.

The geometry of the fibre is divided in two parts, called modules, one aligned with the loading (Module 1 in Fig. 1) and another forming an angle (φ) with the previous one (Module 2 in Fig. 1). The first segment of Module 1 is aligned with the loading direction in order to simulate the experimental setup in which the inclined fibre is clamped in the testing machine and pulled perpendicularly with respect to the crack plane (see for instance Ref. [12]). This makes the initial part of the fibre aligning with the load, and this condition is geometrically represented by the segment 1 of Module 1. Segment 2 in Module 1 represents the actual part of the fibre, which is inclined with respect to the crack plane, whereas, Module 2 represents the geometry of the hook end of the fibre. As per Fig. 1, the fibre embedment length is $L_b = L_{11} + L_{12} + L_{21} + L_{22}$. Throughout this document, the first subscript i is used to indicate module number ($i = 1,2$) and the second subscript j represents each segment of the module ($j = 1,2$).

By modelling each segment of the fibre as a Timoshenko beam, the local balance of shear forces T_{ij} and bending moment M_{ij} of the i-th module, j-th segment is $T' - q = 0$ and $M' - T = 0$, which give the following differential equations that govern the transverse equilibrium:

$$\begin{cases} EI_{ij}\vartheta''_{ij}(x) - K_{ij}\vartheta_{ij}(x) + K_{ij}v_{ij}'(x) = 0 \\ K_{ij}v''_{ij}(x) + q\left(v_{ij}(x)\right) - K_{ij}\vartheta'_{ij}(x) = 0 \end{cases} \tag{1}$$

where $v_{ij}(x)$ is the vertical displacements at x and $\vartheta_{ij}(x)$ is the corresponding rotation of the cross-section (see Fig. A1c for orientation of the reference axis). The other parameters of the model are: I_{ij} the second moment of area of the cross section, $K_{ij} = \kappa A_{ij}G$, $G = E/(2+2\nu)$ the transversal modulus of elasticity of the material ($\nu = 0.3$ for the considered materials), κ the so-called Timoshenko shear coefficient (6/7 for fibres of circular cross section) and A_{ij} the area of the cross section. The function $q(v_{ij})$ is the nonlinear reaction force of the matrix surrounding the fibre and is assumed to be dependent on the transverse displacement and is used to describe damage plastic behaviour of the concrete; as such it is only effective when $v_{ij} > 0$, being 0 otherwise. The model's equation (1) imply the fibre to be modelled as a Timoshenko beam. In fact, it was demonstrated in Ref. [29] that using a Timoshenko model, which accounts for the shear deformability of the fibre, allows a more accurate evaluation of the stress concentration around the fibre

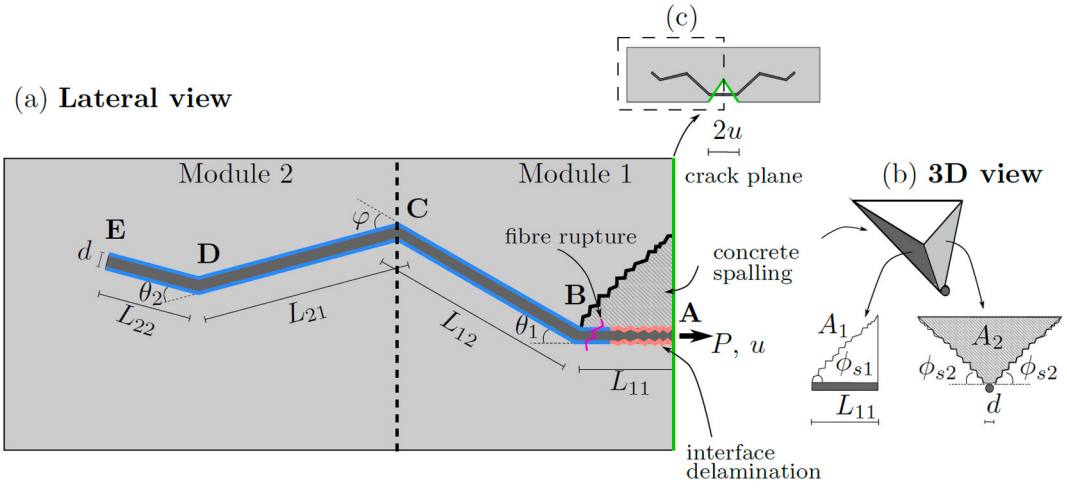

Fig. 1. Main geometric parameters of the microstructural model. The three main failure mechanisms (interface delamination, matrix spalling and fibre rupture) are schematically depicted together with the region where concrete spalling is likely to occur (dashed area between points *A* and *B*).

bending parts (Point B, and C in Fig. 1), compared to simpler Bernoulli-like models. Indeed, in the fibre bending zones, the high stress values, which occur for high inclination angles, are responsible for the micro-cracking of the cement matrix, which in turn may lead to a portion of the matrix to be expunged off during the pull-out of the fibre (Fig. 1).

The horizontal equilibrium at the i-th module and j-th segment is $N'_{ij} = p_{ij}\tau$, which gives the following differential equation of the longitudinal displacement $u_{ij}(x)$

$$u''_{ij}(x) = \frac{p_{ij}}{A_{ij}E}\tau\left(u_{ij}(x)\right), \tag{2}$$

where p_{ij} is the perimeter of the cross-section. Equation (2) was derived by imposing the force equilibrium along the fibre axis and by neglecting the longitudinal deformation of the concrete, which is in any case small compared to the shear deformability of the interface.

In order to solve the differential equations (1) and (2), the constitutive relationships for $\tau(u_{ij})$ and $q(v_{ij})$ must be specified, as well as the boundary conditions for each fibre segments (see the Appendix). In this work, the following cohesive-like trilinear laws (Fig. 2) are assumed:

$$\tau\left(u_{ij}\right) = \begin{cases} \tau_m \dfrac{u_{ij}}{u_I} & \text{if } u_{ij} \le u_I \\ \tau_m & \text{if } u_I < u_{ij} \le u_{II} \\ \tau_r + (\tau_m - \tau_r)\dfrac{u_{II}}{u_{ij}} & \text{if } u_{ij} > u_{II} \end{cases}, \tag{3}$$

$$q\left(v_{ij}\right) = \begin{cases} Kv_{ij} & \text{if } 0 < v_{ij} \le v_I \\ Kv_I & \text{if } v_I < v_{ij} \le v_{II} \\ Kv_I\dfrac{v_{II}}{v_{ij}} & \text{if } v_{ij} > v_{II} \end{cases}, \tag{4}$$

where τ_m/u_I and K are the elastic stiffness of the interface and the foundation, respectively, whereas u_I and v_I represent the sliding at the attainment of the bond strength and the deformability of the fibre's surrounding medium at the attainment of its strength. These values influence the maximum force achieved in the overall force-displacement diagram. In Refs. [29], it was observed that the peak pull-out force decreases for increasing fibre inclination angles. This is mainly due to the matrix spalling at fibre exit point, whose tendency to occur increases with the fibre inclination towards the crack plane. In particular, the matrix spalling causes the effective embedment length of the fibre to decrease, due to the rigid movement of this fibre's part in consequence of the expunged part of matrix. To capture this behaviour, the parameter u_I of the bond-stress constitutive law is made dependent on the angle θ_1 (Fig. 1) by the relationships $u_I = u_I^0 exp(\delta\,\theta_1)$, where δ is used to adjust the dependence of the sliding u_I with the fibre angle θ_1, and u_I^0 is the displacement for $\theta_1 = 0°$, as indicated in Table 2. Consequently, the first branch of the bond interface law has a decreasing stiffness for increasing θ_1; this simple strategy allows the complex micro-mechanisms responsible of the matrix spalling to be simulated.

The constitutive behaviour of the fibre is assumed *brittle*, which is typical of high strength metallic fibre due to the high carbon content. Failure occurs when the axial N_{ij} and shear T_{ij} forces and bending moment M_{ij} verify the following condition

$$\frac{N_{ij}}{N_u} + \frac{V_{ij}}{V_u} + \frac{M_{ij}}{M_u} \ge 1 \tag{5}$$

being N_u, V_u and M_u the axial and shear forces and bending moment at the ultimate limit state. For the fibre type of circular cross-section herein considered, these are:

$$N_u = \sigma_u A_{ij}, \quad V_u = \sigma_u A_{ij}\Big/\sqrt{3}, \quad M_u = 4\sigma_u r_{ij}^3\Big/3, \tag{6}$$

where σ_u is the fibre tensile strength and r_{ij} is the fibre radius at all segments $ij = \{11, 12, 21, 22\}$. On the other hand, if Eq. (5) is not satisfied, debonding occurs. The yield-like criterion (6) was successfully applied in Ref. [24] to model high strength steel fibres; however different type of failure conditions, such as brittle failure, can be easily accounted for in the modelling.

In addition, due to the local curvature and stretching of the fibre close to the fibre exit point, a portion of the matrix could be expunged off from the system, a phenomenon often indicated as *matrix spalling*. The volume of this region depends on the matrix properties, as well as fibre cross section, inclination angle and external force. When the transverse force exerted on the matrix is lower than a critical resistant value, spalling could not occur [21]. Therefore, the evaluation of matrix spalling is carried out by:

$$V_{12}(L_{12}) > R_{sp} \quad with \quad R_{sp} = (A_1 + A_2)f_{ct}, \tag{7}$$

being $V_{12}(L_{12})$ the shear force acting at the connection between the horizontal and inclined segments of Module 1 (in Fig. 1) and f_{ct} is the concrete strength. The variables A_1 and A_2 are the lateral and front areas of the spalling volume, which are related to the fibre orientation θ_1 and the other geometric parameters by:

$$\begin{aligned} A_1 &= L_{11}(L_{11}tan(\phi_{s1}) + d), \\ A_2 &= L_{11}^2 tan(\phi_{s1})\sqrt{2}, \end{aligned} \tag{8}$$

and depend on the relative inclination ϕ_{s1} of the fractured surface of the spalled volume and the fibre; the crack is assumed to propagate perpendicularly to the inclined part of the reinforcement, thus $\phi_{s1} = \pi/2 - \theta_1$. The angle ϕ_{s2} in Fig. 1b represents the inclination of the fracture surfaces of the spalled concrete volume, which is assumed to be 45°, as proposed in Refs. [21]. This assumption is reasonable, since 45° is approximately the internal frictional angle of fracture in cement-based materials.

2.1. Calibration of the microstructural model

In this section, the microstructural model is calibrated by using the experimental results on the new generation of hooked-end steel fibres tested in Ref. [12], as well as other results available from the open literature [17–19]. The collected data considers hooked end fibres with

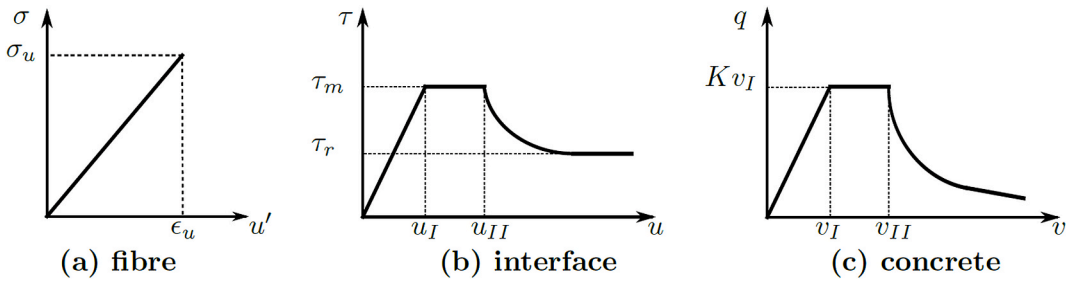

Fig. 2. Constitutive laws used to the describe the behaviour of the fibre (a), of the interface (b) and the concrete (c).

different diameter, tensile strength and embedment length and also different types of cement matrix. The main features of these experiments are summarised in Table 1, where specimen Lb20-C and Lb30-C refers to data in Ref. [12], Lb15-R in Ref. [18], Lb20-S in Ref. [19] and Lb-K in Ref. [17]. It is noted that, in all the experiments considered, the fibres had a certain inclination towards the crack plane (θ_1 in Table 1 and Fig. 1), while a horizontal segment with minimal length of $L_{11} = 1$ mm was considered in the modelling for simulating the real testing conditions.

The values of the constitutive parameters were obtained by fitting, for each of the available specimen, data for all angles and embedment lengths simultaneously. To do that, the model was implemented in Matlab and the nonlinear differential equations ((1) and Eq. (2)) were solved numerically through an iterative algorithm; details on the numerical procedure can be found in Ref. [29]. At each iteration, the values of axial N_{ij} and shear V_{ij} forces, and the bending moment M_{ij} were evaluated and the type of failure mode assessed through Eqs. (5)–(7). The matrix spalling occurs when Eq. (7) is verified, and, in such a case, the horizontal length (L_{11}) of the reinforcement is made unbonded by letting to zero the support reaction q in Eq. (1), meaning that no lateral force is transferred to the fibre in the spalled region. Two stopping conditions for the numerical algorithm were implemented, one occurring when $N_{ij}/N_u + V_{ij}/V_u + M_{ij}/M_u = 1$, that is the hooked fibre has failed by tensile rupture, the other when the entire fibre-matrix interface is in softening (complete sliding of the fibre). It is noted that, in the proposed approach, the spalling of the matrix represented by condition (7), always occurs in conjunction to debonding or rupture of the fibre as, indeed, it was experimentally observed in Ref. [12].

Table 2 lists the results of the fitting for all the experiments considered, whereas a detailed description of the results is given in the rest of this section.

In [19], the pull-out tests of hooked end fibres with 0.75 mm of diameter and three different embedment lengths $L_b = 10, 20, 30$ mm were performed.

The results of the fitting, shown in Fig. 3a, shows that the model simulates accurately the fibre pull-out response of the tested fibres regardless the fibre embedment length considered. It shows that at higher inclination angles, the displacement at peak force is drastically increased due to the different degradation mechanisms that governs the response: at lower angles, fibre sliding is the mandatory mechanism, whereas, at higher angles, damage starts accumulating at the transition zone between horizontal and inclined segments and lead to matrix spalling and eventually to fibre rupture. Moreover, the model was also used for modelling the pull-out of aligned hooked end fibres with three embedments lengths ($L_b = 10$, 20, 30 mm) carried out by Ref. [17]. The authors used steel fibres with hooked ends, where the total length (L_f) of the fibre equals to 50 mm and the fibre diameter is 0.75 mm, and the tensile strength of the steel fibre is equal to 1100 MPa. The good agreement between the analytical model and the experimental results in Ref. [17] is seen in Fig. 3b for different embedment lengths.

To further asses the capabilities of the proposed model, the data from Ref. [18] and the corresponding prediction from the model are shown in Fig. 4. In these experiments, fibres of 0.50 mm diameter and 15 mm embedment length were pulled out from concrete specimens of 72 MPa compressive strength, oriented towards the crack plane at 0°, 10°, 30°, 40°, 50° and 60°. At lower orientations, the friction resistance in the straight parts of the fibre and mobilisation and straightening of the hooked end have the major influence on the pull-out response. At higher angles, the energy absorption capacity seems to be overestimated by the model. Since this fibre has a smaller diameter, thus a lower stiffness, the Winkler foundation model may be less accurate to describe this type of system; in fact, Winkler hypothesis is known to be valid when the beam's (the fibre in the present case) stiffness resting in the foundation had at least one order of magnitude higher stiffness than concrete. Moreover, when the matrix spalling occurs, the fibre embedment length is reduced and the original inclination angle changes; this behaviour is not well captured by the model, since only a fixed inclination angle is considered and eventual plastic deformation on the curvature zones is neglected.

For the case of concrete strength, fibre type and embedment length ($L_b = 15$ mm) adopted in the tests of [18], the peak pull-out load of a hooked end fibre is maximum at 30° orientation. In a similar way as the previous results, the displacement/slip at which peak-load occurs increases with fibre orientation. For fibres that fail by tensile rupture, the fracture load decreases with the increase of the fibre orientation. In terms of the pull-out energy absorption of a hooked end fibre, if fibre does not fail by tensile rupture, an inclined fibre with respect to the loading direction absorbs a greater amount of energy at a given displacement than one that is aligned, with a maximum value occurring between 10 and 30° to the direction of loading (see Fig. 4). Fig. 5 shows the normalised axial stress (σ_f) variation along the hooked end fibre ($L_b = 15$ mm) for two orientation angles, namely: $\theta_1 = 10°$ (Fig. 5a) and $\theta_1 = 60°$ (Fig. 5b). The stress field along the fibre shows that the hooked end contributes to the pull-out resistance and indeed a higher stress in the hook is achieved for 10° fibre compared to 60° fibre. This can be explained by the lower pull-out force for the higher angles, since the stress concentration at the loaded end leads to the premature fibre rupture. Correspondingly, the 60° fibre attains a pull-out force lower that the one of the fibre at 10°.

Finally, the hooked-end fibre used in Ref. [12] had a diameter 0.75 mm and was embedded into a self-compacting concrete with 83.4 MPa compressive strength. The embedment lengths $L_b = \{20.0, 30.0\}$ mm and the inclination angles 0, 30 and 60° were tested. The results in Fig. 6 show the high accuracy in the fitting of both peak force and loaded-end slip for all fibre orientations and fibre embedment lengths. The pull-out response is made up of three parts, a feature common to all the experimental data considered. For 0° and 30°, the hooked end has a limited impact on the initial response, and, in fact, the peak force is achieved almost at the same loaded end slip values. However, for the fibre oriented at the highest inclination (60°), the pressure introduced by the fibre in the matrix at the exit point region is so intense that matrix spalling occurs, which is associated to a significant stiffness decrease. During this spalling process, the fibre in this region has moved in order to be aligned with the loading direction, which has increased the shear force and the bending moment, leading to the tensile rupture of the fibre that occurred at larger loaded end slip than the other fibre orientations (governed by Eq. (5)). The post-peak behaviour of the specimen differs

Table 1
Geometric parameters for modelling the inclined hooked end fibre, being $ij = \{11,12,21,22\}$.

Specimen	Citation	L_{11} [mm]	L_{12} [mm]	L_{21} [mm]	L_{22} [mm]	θ_1 [°]	φ [°]	θ_2 [°]	A_{ij} [mm^2]	p_{ij} [mm]
Lb15-C	[12]	1	9.5	2.5	2.2	0, 30, 60	42	41	0.48	2.56
Lb20-C	[12]	1	14.5	2.5	2.2	0, 30, 60	42	41	0.48	2.56
Lb30-C	[12]	1	24.5	2.5	2.2	0, 30, 60	42	41	0.48	2.56
Lb15-R	[18]	1	10.4	2.2	1.4	0 – 60	45	45	0.19	1.57
Lb20-S	[19]	1	15.9	1.8	1.3	0, 30, 60	44	42	0.48	2.56
Lb-K	[17]	1	5, 15, 25	2.5	1.5	0	45	45	0.48	2.56

Table 2
Material parameters for fibre concrete composite for the different experiments in Table 1.

Specimen	E	σ_u	τ_m	τ_r	u_I^0	δ	u_{II}	K	v_I	v_{II}
	GPa	MPa	MPa	MPa	[mm]	–	[mm]	GPa	[mm]	[mm]
Lb15,20,30-C	200	1200	2.05	0.90	0.20	1.5	$1.3u_I$	20	0.17	0.25
Lb15-R	200	1100	1.65	0.75	0.30	1.7	$1.2u_I$	15	0.12	0.18
Lb20-S	210	2200	1.70	0.42	0.38	1.4	$1.2u_I$	12	0.14	0.22
Lb-K	210	1100	1.85	0.65	0.27	1.6	$1.4u_I$	13	0.11	0.19

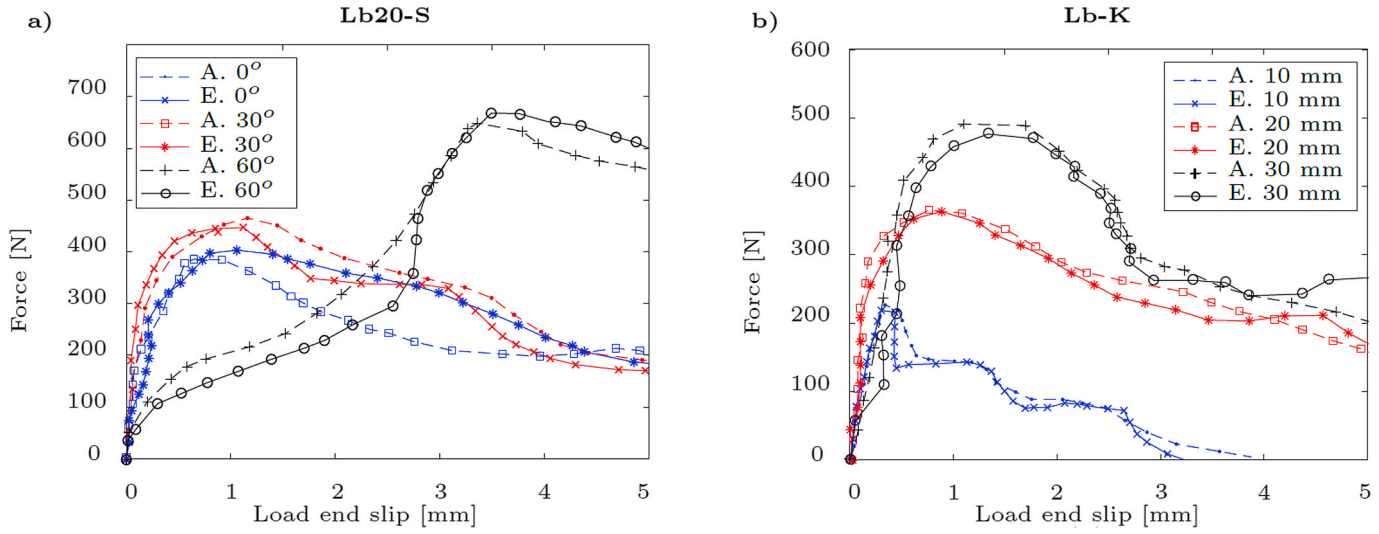

Fig. 3. Force vs. displacement obtained by fitting the analytical model to data in Ref. [19] (a) and [17] (b) (A. = Analytical; E. = Experimental).

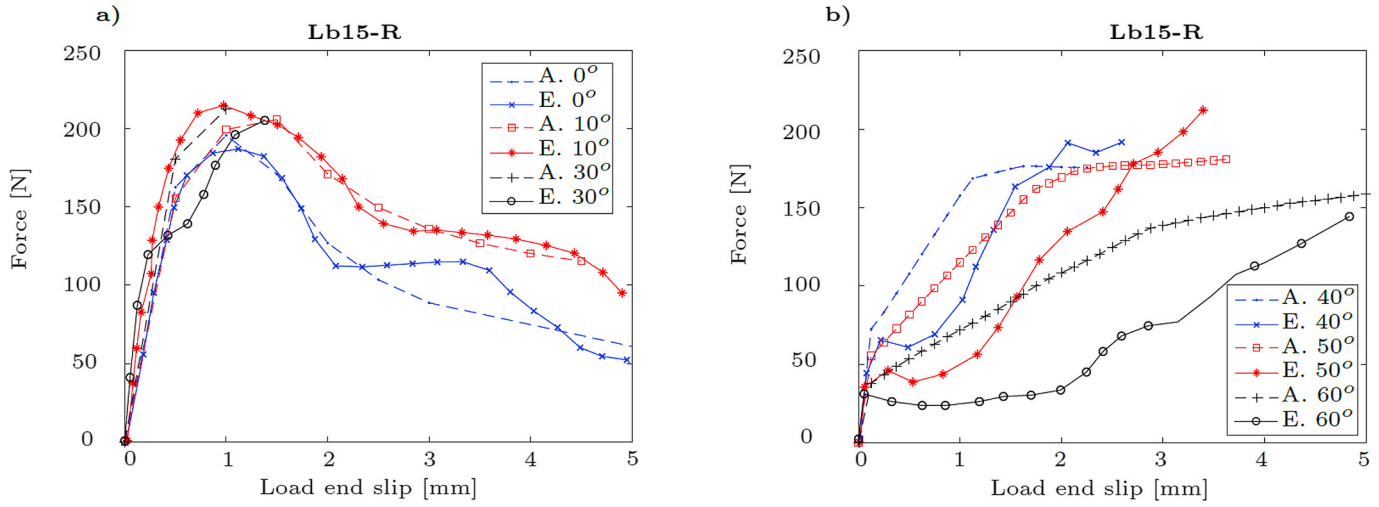

Fig. 4. Force vs displacement obtained by fitting the analytical model to the experimental data from Ref. [18] with $L_b = 15$ mm. (A. = Analytical; E. = Experimental).

significantly among the specimens. In both cases ($L_b = \{20.0,30.0\}$ mm), the ascending branch of the 30° fibre is not so pronounced, due to the small amount of cracking and spalling of the matrix at the fibre exit point, caused by a relative higher stress concentration in the transition zone than the one of the aligned fibre. Although a small post-peak load decaying is also ob-served for 0° specimen at displacement around 1 mm, this is caused by the frictional resistance of the surrounding matrix, which is again well matched by the model. Remarkably, the model is able to describe with the same set of parameters the three angles as well as the two embedment lengths taken into account. The results show that the load end slip at peak load increases more than the inclination angle, which is due to a combination of concrete softening and fibre straightening effects that takes place during the test at fibre curvature zone close to the load point, thus increasing the measured fibre displacement. This load drop leads to a significant loss of stiffness that was well represented by the proposed model. As seen, the model reproduces accurately the behaviour for the tree angles fibres analysed, irrespectively of the occurrence of matrix spalling. In the next section, by using the constitutive parameters for the hooked-end fibre used in Ref. [12], a macro-scale model will be developed to simulate the flexural capacity of a SFRC beam from Ref. [30].

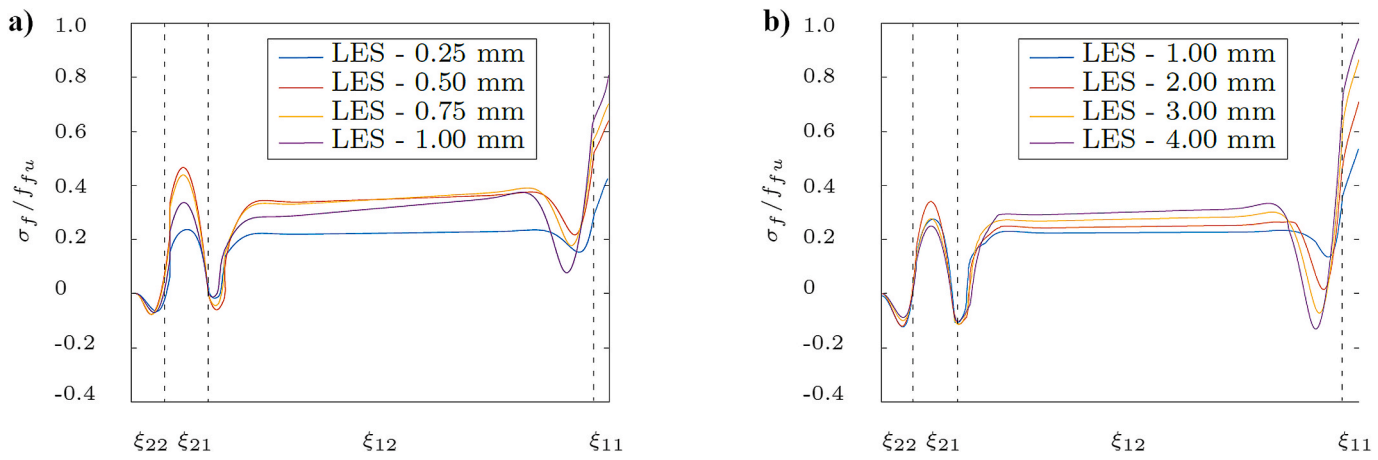

Fig. 5. Variation of the normalised axial stress along the fibre for the hooked end system ($L_b = 15$ mm) from Ref. [18] with $\theta_1 = 10°$ (a) and $\theta_1 = 60°$ (b). In the legend, LES is the Load End Slip.

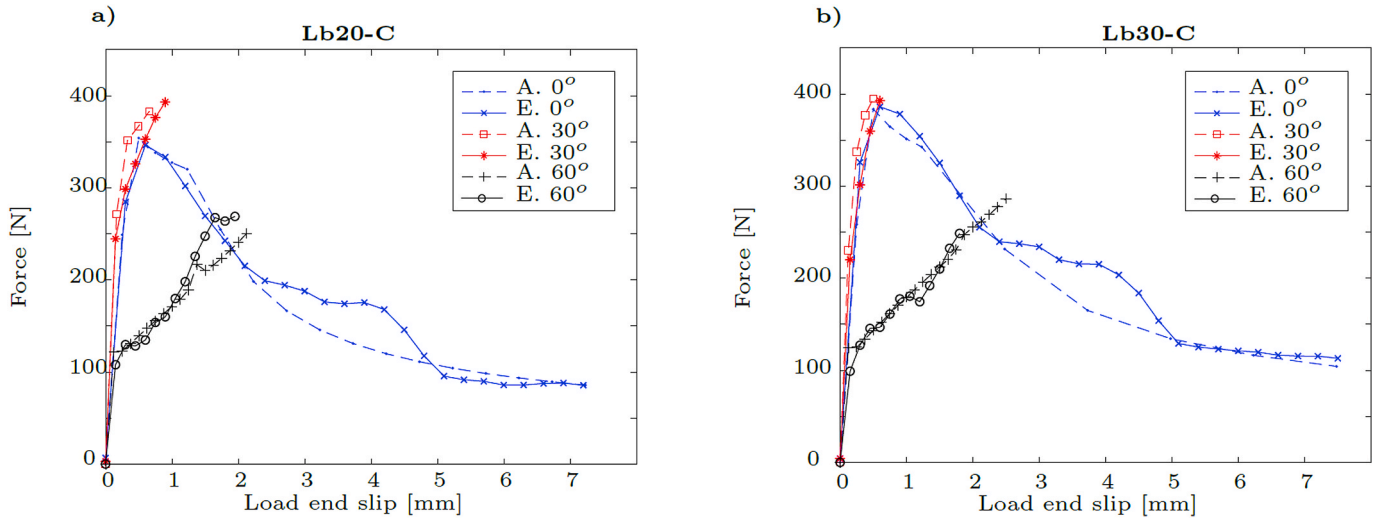

Fig. 6. Force vs displacement obtained by fitting the analytical model to the experimental data from Ref. [12] with $L_b = 20$ mm (a) and $L_b = 30$ mm (b).

3. Macroscopic model for predicting flexural capacity of FRC structural elements

The present section aims at integrating the fibre pull-out constitutive laws, derived from the model described in Section 2, within an approach that considers the fibre orientation profile in a SFRC cracked section for estimating the flexural capacity of a SFRC structural element. This approach is inspired by the shear model developed in Refs. [26] and applied to predicting the shear capacity of SFRC beams flexurally reinforced with conventional steel bars. The fibre orientation profile, fibre distribution and the local bond-law are coupled to form a new material model to simulate the nonlinear material behaviour of FRC cross section of an element failing in bending. This approach is described, and its predictive performance is assessed by simulating three-point notched beam bending tests (3PNBBT) carried out in Ref. [30] with steel fibre reinforced self-compacting concrete (SFRSCC). The type of fibres and concrete used in the test are the Lb15-C in Table 1, whose mechanical properties are listed in Table 2.

3.1. Description of the numerical approach

The integrated model was implemented in DOCROS, an already existing software for the analysis of cross-sections of members failing in bending [31]. In DOCROS a cross-section is discretized in layers, and for each layer a specific constitutive law is assigned to describe the behaviour of materials representing the layers (more than on material can exist in a layer). The cross section is assumed to remain plane since the number and stiffness of the fibres crossing the cross section do not have influence to invalidate this assumption. For the simulation of the tensile behaviour of the FRC, a linear elastic stress-strain response is considered up to the concrete tensile strength, f_{ct}. For the post-cracking tensile response, the contribution of the fibre pull-out resistance, P_w, is added to the post-cracking residual strength of the FRC matrix, $\sigma_{ct}(w)$, namely:

$$\sigma^j = \frac{P^j(w^j)}{b^j t^j} + \sigma^j_{ct}(w^j) \tag{9}$$

where b^j and t^j are, respectively, the width and thickness of a generic j-th layer, and w^j is the crack width at the level of the geometric centre of the j-th layer. The adopted stress-crack width relationship of the concrete matrix is based on the model presented in Ref. [32]. For usual fibre dosages used in FRC, the compressive behaviour is similar to the one observed in plain concrete, and so the behaviour of FRC in compression was simulated by adopting the model proposed in Ref. [33].

The distribution of orientation angles of the fibres, ϕ, is determined according to the model proposed in Ref. [27]. The number of fibres at the crack plane is determined considering the fibre orientation factor, η

[30]. Afterwards, the fibre orientation domain is arranged in discrete intervals, $\eta\Delta\phi$, and the number of fibres within each orientation angle interval is determined by assuming a Gaussian distribution of the angles.

The fibre distribution model can be used to simulate fibre segregation that can occur during FRC casting, by capturing the variation of the number of fibres along the depth of the cross section [28]. In fact, by considering that the cross-section of a FRC member is discretized in N layers ($j = 1, \ldots, N$), and that the fibre orientation domain is divided into $i = 1, \ldots, \eta\Delta\phi$ intervals, at the j-th cracked layer of the cross-section, the fibre pull-out resistance is equal to:

$$P^j(w) = \sum_{i=1}^{\eta\Delta\phi} P^j_{\overline{\phi}_i}(w) \tag{10}$$

$$P^j_{\overline{\phi}_i}(w) = N^j_{f,\overline{\phi}_i} \; P_{\overline{\phi}}(u = w) \tag{11}$$

where $P^j_{\overline{\phi}_i}(w)$ is the pull-out resistance of the $N^j_{f,\overline{\phi}}$ fibres with a mean orientation angle $\overline{\phi}$ at the j-th cracked layer, determined according to the fibre orientation and segregation model; $P_{\overline{\phi}}(u)$ is the fibre pull-out resistance of a fibre with an orientation angle $\overline{\phi}$, which is a function of the slip at the loaded end, u, and is obtained from the model presented in Section 2, for which $\theta_1 = \overline{\phi}$. The present model follows the assumption that the fibre slip from the matrix occurs from the shorter embedded length of the fibre, and the slip between the longer embedded part of the fibre and its surrounding matrix is negligible. Therefore, it is assumed that the slip of the shorter embedded length is equal to the crack opening displacement at each layer, $u = w$.

In Fig. 7 is schematically presented an example of the calculation of the pull-out force of the fibres bridging the crack at the jth cracked layer of a FRC cross-section. Assuming the domain of fibre orientation is decomposed in four equal intervals ($n\Delta\phi = 4$; $\Delta\phi_i = 22.5^o$), the $P^j_{\overline{\phi}_i}(w)$ is obtained in the middle of each interval by considering the number of fibres with orientation in this interval, therefore Eq (10) becomes:

$$P^j(w) = P^j_{\overline{\phi}_i=11.25^o}(w) + P^j_{\overline{\phi}_i=33.75^o}(w) + P^j_{\overline{\phi}_i=56.25^o}(w) + P^j_{\overline{\phi}_i=78.75^o}(w) \tag{12}$$

For deriving the moment-rotation approach, for an imposed rotation in the cracked section, the position of the neutral axis is evaluated by assuring the equilibrium of axial forces in the cross section. Then, the corresponding bending moment is determined considering the contribution of the concrete and fibres for each layer of the cross section.

4. Assessment of the predictive performance of the model

The predictive performance of the proposed integrated model is assessed by simulating the series of 3PNBBT carried out by Cunha [30], with self-compacting concrete reinforced with 30 kg/m^3 of the hooked-end steel fibres of the following properties: $L_f = 60$ mm, $d_f = 0.75$ mm, $E = 200$ GPa and $\sigma_u = 1200$ MPa. According to the data published in, the SFRSCC has presented the following average mechanical properties: compressive strength of $f_{cm} = 71.1$ MPa, tensile strength of $f_{ctm} = 3.6$ MPa and Young modulus of $E_{cm} = 41.5$ GPa.

By dividing the fibre orientation profile in 6 intervals ($\eta\Delta\phi = 6$), i.e. 15° for each one, the pull-out constitutive laws for the fibres representing each of these intervals ($\overline{\phi} = 7.5^o$, $\overline{\phi} = 22.5^o$, $\overline{\phi} = 37.5^o$, $\overline{\phi} = 52.5^o$, $\overline{\phi} = 67.5^o$, and $\overline{\phi} = 82.5^o$) were obtained by applying the model of Section 2, whose geometric and material parameters are indicated as Lb15-C in Tables 1 and 2 $\theta_1 = \overline{\phi}$. Due to convergence difficulties on obtaining the fibre pull-out constitutive law for the average fibre orientation $\overline{\phi} = 82.5^o$, and considering the fibres at this interval are of small number and give relatively small contribution, this constitutive law was determined according to the pull-out constitutive model presented in Ref. [28]. According to Ref. [34], the shorter fibre embedded length (L_b) in SFRC can be considered equal to $L_f/4 = 15$ mm, thereby $L_b = L_{11} + L_{12} + L_{21} + L_{22} = 15$ mm (Fig. 1). The obtained fibre pull-out constitutive laws are represented in Fig. 8a.

For the numerical simulation of the SFRSCC notched beams, the crosssection was discretized in 125 layers, with 1 mm of thickness and 150 mm of width. As the experimental program has followed the recommendations of the standard [35], it can be assumed a uniform distribution of the fibres along the cross-section height. According to the image analysis conducted by Cunha [30], a fibre orientation factor equal to $\eta = 0.768$ was obtained at the notched section of the beams, which was considered in the fibre orientation model implemented in DOCROS.

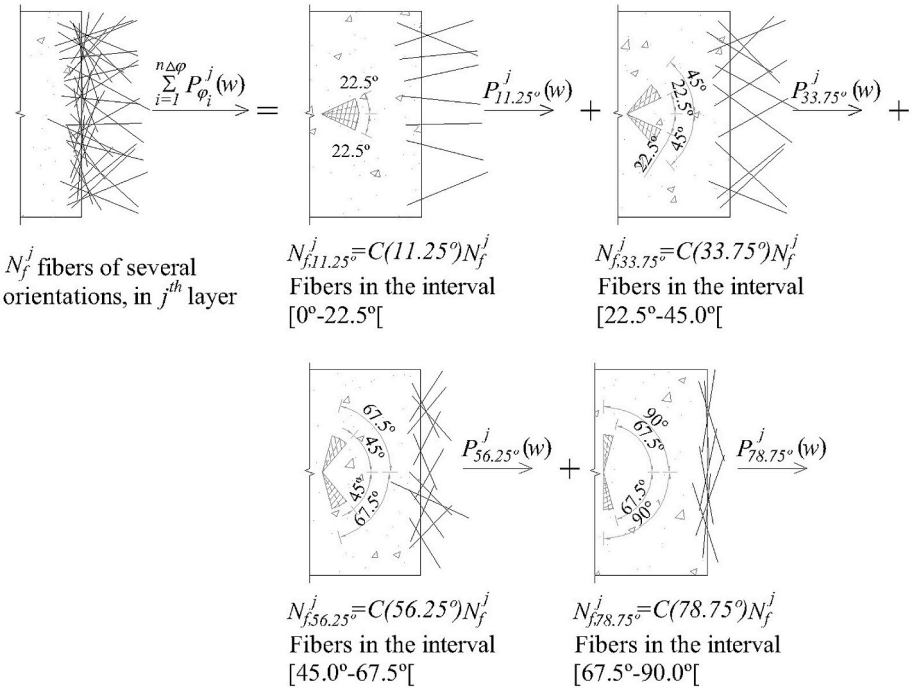

Fig. 7. Example to calculation of the fibre pull-out force at jth cracked layer, considering $n\Delta\phi = 4$; $\Delta\phi_i = 22.5^o$.

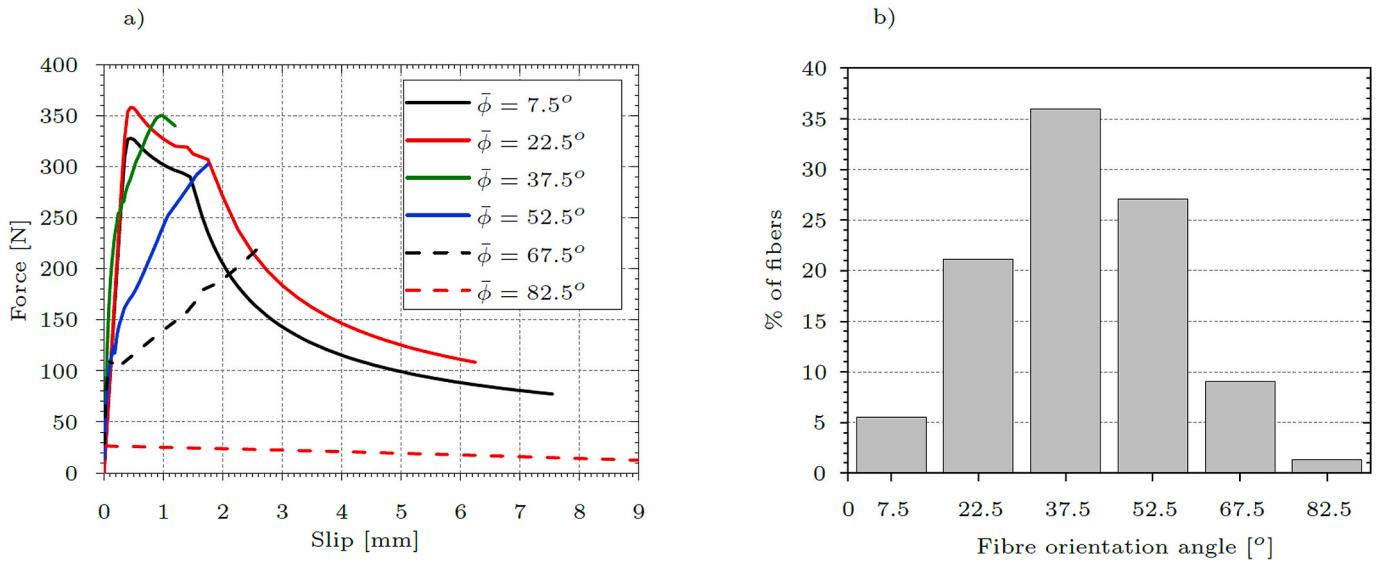

Fig. 8. a) Fibre pull-out constitutive laws for the fibre orientation intervals considered; b) Fibre orientation profile in the simulated beams.

According to the fibre orientation and distribution models, 124 fibres are bridging the cross-section with the orientation profile presented in Fig. 8b.

The moment vs. rotation relationship for the cross-section at the notched plane is obtained from DOCROS. In order to derive the force vs. deflection relationship of the 3PNBBT, the formation of a nonlinear hinge is assumed (Fig. 9a), with a length equal to the height of the fracture surface ($2l_2 = h$), subjected to an equivalent uniform bending moment, M_u, that is related to the applied force, F, as per

$$M_u = \frac{F}{4}(L - l_2) \tag{13}$$

The deflection δ of the 3PNBBT is determined assuming the superimposition of the elastic δ_{el} and plastic δ_{pl} vertical deformation of the beam at the midspan, i.e., $\delta = \delta_{el} + \delta_{pl}$. The two components of the deflection are schematised in Fig. 9b and c, respectively, and can be determined from the following equations:

$$\delta_{el} = \frac{F}{2E_c I_2}\left(\frac{l_2^3}{3} + l_2^2 l_1 + l_1^2 l_2 + \frac{l_1^3 I_2}{3\, I_1}\right); \qquad \delta_{pl} = \frac{2L\vartheta}{4} \tag{14}$$

where ϑ is the rotation of the beam, I_1 and I_2 are the second moment of inertia of each segment of the beam, namely: $I_1 = bH^3/12$, $I_2 = bh^3/12$.

In Fig. 10a is compared the experimental and numerical response of the force vs. deflection relationship of the SFRSCC beams submitted to 3point bending loading configuration. As can be seen, the initial numerical curve [Numerical ($\kappa = 1.0$)] is within the experimental envelope for deflection values higher than 1.2 mm, by approaching the

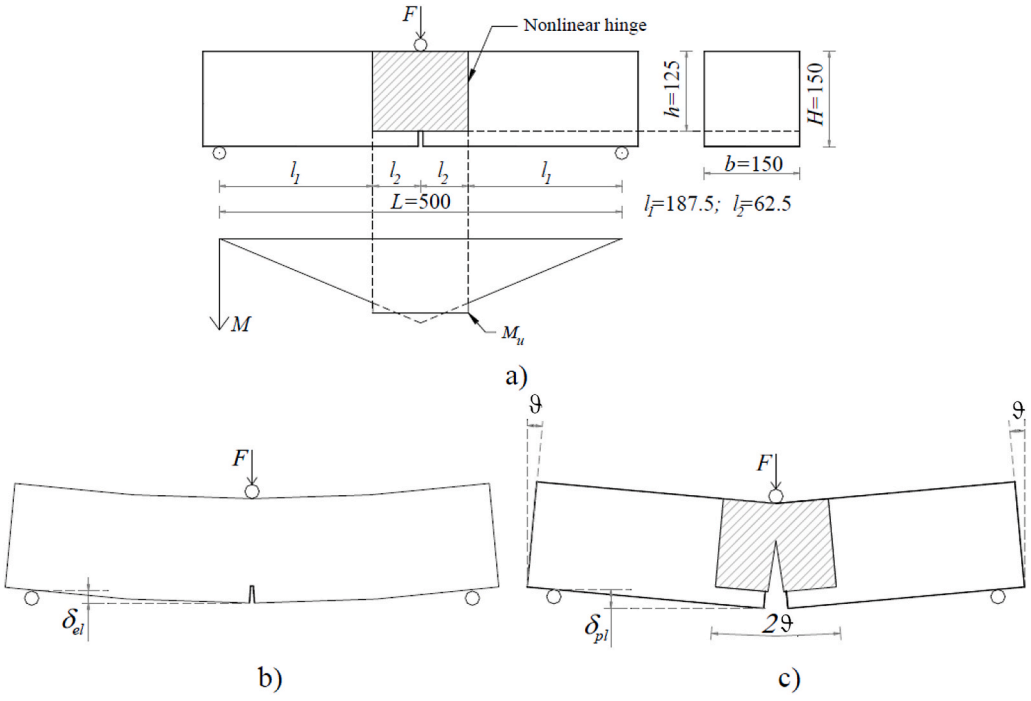

Fig. 9. a) Nonlinear hinge formed in the 3PNBBT and its uniform equivalent bending moment; b) elastic deflection of the beam; c) plastic deflection of the beam (dimensions in mm).

experimental average curve with the increase of the deflection. However, up to the aforementioned deflection level, the numerical response predicts a load carrying capacity lower than the one recorded experimentally. This difference can be justified by the simplifications adopted in the numerical simulation. In fact, the force-deflection relationship was determined from the bending moment-rotation response of a cross section assumed smooth, corresponding to the notched section of 125 × 150 mm^2. Therefore, it is assumed that the crack starts at the notch tip and propagates vertically along the notched section. However, in the experimental tests the crack along the notched cross-section constantly changes direction and can bifurcate in two or more cracks (Fig. 10b), due to the intrinsic heterogeneous nature of the FRC material structure [37]. This cracking ramification is expected to increase with the percentage, length, and aspect ratio of the fibres, as well as with the concrete strength. This cracking ramification can increase significantly the total fracture surface area formed, by absorbing a higher fracture energy in the cracking process of the concrete and pulling out a higher number of fibres. This leads to a higher load carrying capacity than when assumed the fracture is restricted to the notched plane. In order to simulate the effect of cracking diffusivity, the theoretical fracture surface is multiplied by a related factor, κ. When the content of fibres decreases, the κ factor tends to the unitary value. In the extreme case of plain concrete (without fibres), $\kappa \approx 1.0$ (some tortuosity always exists due to the present of aggregates), since the assumed perfectly smooth surface is approximately the real case scenario. In the present case, this parameter was added to the numerical model, and by considering $\kappa = 1.35$, as presented in Fig. 10a, it is obtained a numerical optimized force vs. deflection relationship with a very good agreement with the experimental average curve. These results clearly justify the nonconservative predictions of the load carrying capacity of SFRC structures when the stress-crack width constitutive law of the SFRC is obtained by traditional inverse analysis techniques, since in these techniques the crack propagation is assumed restricted to the notched plane [38]. The proposed method can, therefore, be regarded as an indirect approach for estimating the real total fracture surface that is formed during a 3PNBBT. In the present tests this increase is about 35%.

In Fig. 11 is presented the fibre and matrix contributions to the tensile stress vs. crack width for each layer that discretizes the cross-section (A^j= 150 mm^2) of the SFRSSC beam.

5. Conclusions and future works

An integrated approach to predict the flexural behaviour of FRC beam is proposed in this paper. The pull-out behaviour of the fibre reinforcement was investigated through a microstructural model accounting for the geometry of the hook and the inclination of the fibre towards the crack plane. The fibre is modelled as a one-dimensional continuum for which axial, shear and bending deformability are accounted for. The interaction with the concrete matrix is described by a nonlinear foundation with a cohesive-like constitutive laws used to describe both the fibre-matrix interface and the deformability of concrete in compression. The proposed approach is based on the solution of the differential equations governing the horizontal and transverse forces equilibrium of the fibre and its surrounding medium. The additional complexities induced by the fibre misalignment were considered, including the transverse loading on the interface, bending of the fibre and the damage of the concrete matrix due to spalling. This behaviour is achieved by tuning the cohesive-like interfaces which describe the local interaction of the fibre with the surrounding concrete. Compared to previous literature models, this micromechanical approach incorporates all the three main local failure mechanisms, which are fibre debonding and rupture, matrix spalling.

The microstructural model is incorporated within an integrated approach to simulate the flexural behaviour of SFRC members, which considers the orientation of the fibres, the fibre distribution along the cross-section of these members, and the pull-out response model of each fibre bridging the two faces of a crack. Remarkably, it was shown that by using the experiments on the pull-out of a single fibre for only three angles, 0°, 30° and 60°, the macroscopic model was able to capture with satisfactory accuracy, the behaviour of a concrete beam reinforced with discrete fibres with a Gaussian distribution of the fibre angle. To simulate the cracking diffusivity effect, a parameter (κ) was added to the numerical model, a factor that multiplies the fracture surface, considered $\kappa = 1.35$. This innovative approach can be used for determining, by inverse analysis, the stress-crack width relationship of FRC, which is used in the major part of the FEM-based computer programs for analysis and design of FRC structural elements.

Data availability

Data used in the present paper will be made available upon request.

CRediT authorship contribution statement

C.A. Nonato Da Silva: All authors equally contributed to the manuscript. **J. Ciambella:** All authors equally contributed to the manuscript. **J.A.O. Barros:** All authors equally contributed to the manuscript. **T.D. dos Santos Valente:** All authors equally contributed to the manuscript.

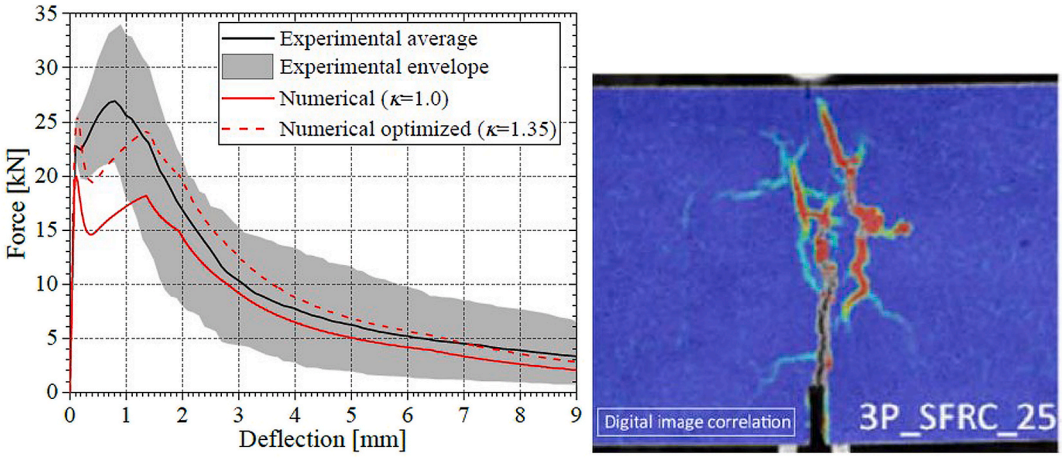

Fig. 10. a) Experimental and numerical model comparison of force vs. deflection relationship for SFRSCC prisms; b) Examples of crack tortuosity and branching of notched FRC prisms submitted to 3-point bending tests (extracted from Ref. [36]).

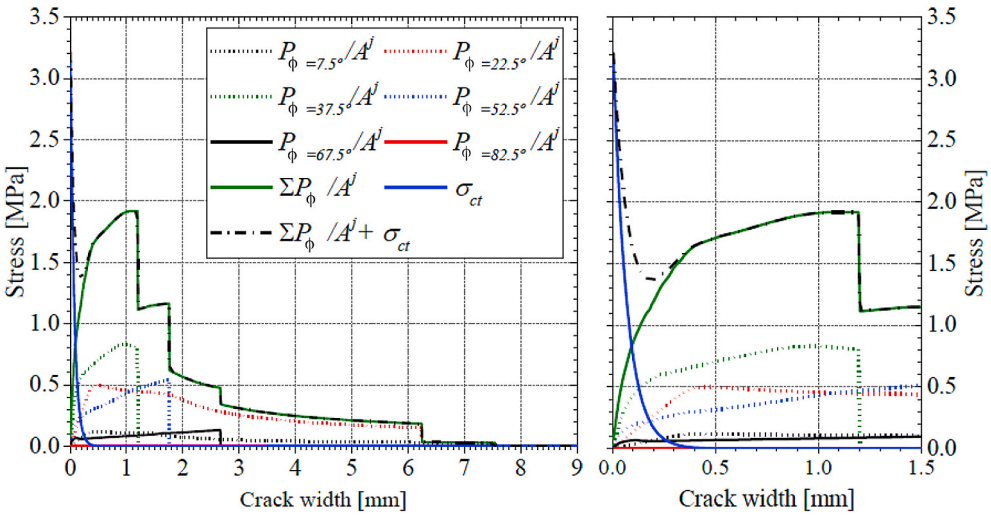

Fig. 11. Contribution of fibres and concrete matrix for the tensile stress of each layer of the cross-section.

Declaration of competing interest

The authors declare that they have no known competing financial interests or personal relationships that could have appeared to influence the work reported in this paper.

Acknowledgements

J.O.A. Barros, T. dos Santos Valente and I. G. Costa wish to acknowledge the support by FEDER through the Operational Program for Competitiveness Factors - COMPETE and Internationalization Program (POCI), under the project NG TPfib POCI-01-0247-FEDER-033719.

Appendix A. Boundary Conditions

In this Section, details on the boundary conditions used to solve the boundary value problem (1)-(2) are given (see also Figure A1). At the end of the fibre, (Point A in Figure A1a), the following conditions are applied:

$$u_{11}(L_{11}) = \overline{u}, \qquad v_{11}(L_{11}) = 0, \qquad \vartheta_{11}(L_{11}) = 0, \tag{A.1}$$

where $\overline{u}$ is the applied displacement, normally designated as loaded end slip (displacement in the present case since negligible deformation for the concrete at reinforcement exit point was assumed) in the reinforcement pullout tests. In cracked cement-based materials, the displacement/slip ($\overline{u}$) can be considered equal to half of the crack width (Fig. 1c). The present model assumes a null vertical displacement in the loaded end in accordance with the boundary conditions experimentally applied in Ref. [12]. Concerning the free end (Point E in Fig. 1a), the following boundary conditions are assumed:

$$N_{22}(0) = 0, \qquad T_{22}(0) = 0, \qquad M_{22}(0) = 0. \tag{A.2}$$

At the connections between the segments (Point B and C in Figure A1a), the continuity of forces/moment yields the following conditions (Point B is showed in Figure A1b):

$$\begin{aligned} N_{11}(0) &= N_{12}(L_{12})cos(\theta_1) - T_{12}(L_{12})sin(\theta_1), \\ T_{11}(0) &= N_{12}(L_{12})sin(\theta_1) + T_{12}(L_{12})cos(\theta_1), \\ M_{11}(0) &= M_{12}(L_{12}). \end{aligned} \tag{A.3}$$

$$\begin{aligned} N_{12}(0) &= N_{21}(L_{21})\cos(\varphi) - T_{21}(L_{21})\sin(\varphi), \\ T_{12}(0) &= N_{21}(L_{21})\sin(\varphi) + T_{21}(L_{21})\cos(\varphi), \\ M_{12}(0) &= M_{21}(L_{21}) \end{aligned} \tag{A.4}$$

$$\begin{aligned} N_{21}(0) &= N_{22}(L_{22})cos(\theta_2) - T_{22}(L_{22})sin(\theta_2), \\ T_{21}(0) &= N_{22}(L_{22})sin(\theta_2) + T_{22}(L_{22})cos(\theta_2), \\ M_{21}(0) &= M_{22}(L_{22}). \end{aligned} \tag{A.5}$$

together with the continuity of displacements/rotations (Point B is showed in Figure A1c):

$$\begin{aligned} u_{11}(0) &= u_{12}(L_{12})cos(\theta_1) - v_{12}(L_{12})sin(\theta_1), \\ v_{11}(0) &= u_{12}(L_{12})sin(\theta_1) + v_{12}(L_{12})cos(\theta_1), \\ \theta_{11}(0) &= \theta_{12}(L_{12}). \end{aligned} \tag{A.6}$$

$$\begin{aligned} u_{12}(0) &= u_{21}(L_{21})\cos(\varphi) - v_{21}(L_{21})\sin(\varphi), \\ v_{12}(0) &= u_{21}(L_{21})\sin(\varphi) + v_{21}(L_{21})\cos(\varphi), \\ \theta_{12}(0) &= \theta_{21}(L_{21}) \end{aligned} \tag{A.7}$$

$$
\begin{aligned}
u_{21}(0) &= u_{22}(L_{22})cos(\theta_2) - v_{22}(L_{22})sin(\theta_2),\\
v_{21}(0) &= u_{22}(L_{22})sin(\theta_2) + v_{22}(L_{22})cos(\theta_2),\\
\theta_{21}(0) &= \theta_{22}(L_{22}).
\end{aligned}
\tag{A.8}
$$

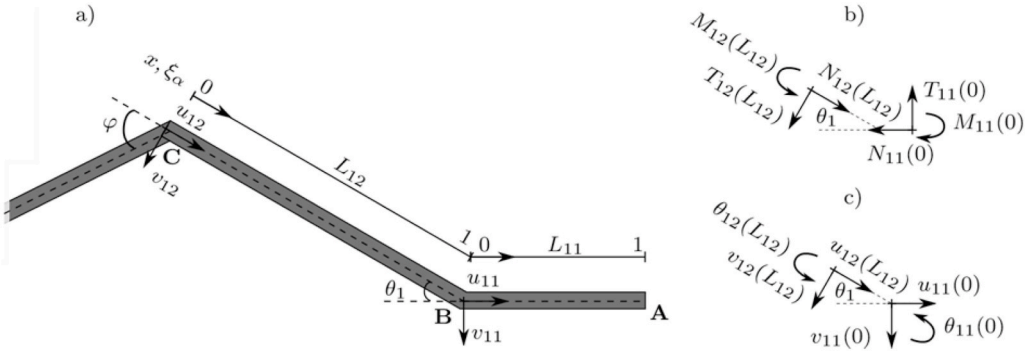

Figure A.1. a) Free body diagram of the system and b) force balance and c) displacement continuity of the hooked end model.

References

[1] Bentur A, Mindess S. Fibre reinforced cementitious composites. second ed. UK: Francis & Taylor; 2007.
[2] Conforti A, Tiberti G, Plizzari GA, Caratelli A, Meda A. Precast tunnel segments reinforced by macro-synthetic fibers. Tunn Undergr Space Technol 2017;63:1–11.
[3] Soetens T. Design models for the shear strength of prestressed precast steel fibre reinforced concrete girders. Ph.D. thesis. Ghent University; 2015.
[4] Gonilha JA, Barros JAO, Correia JR, Sena-Cruz J, Branco FA, R LF, Gonçalves D, Alvim MR, Santos T. Static, dynamic and creep behaviour of a full-scale gfrp-sfrscc hybrid footbridge. Compos Struct 2014;118:496–509.
[5] Mobasher B, Barros JAO, Naaman AE, Destree X. Report on design and construction of steel fiber-reinforced concrete elevated slabs. In: ACI 544.6r-15, reported by ACI committee 544. American Concrete Institute; 2015.
[6] Barros JAO. Fiber reinforced concrete and glass fibre reinforced polymer systems for the development of more sustainable construction systems. In: 9th RILEM international symposium on fiber reinforced concrete. BEFIB 2016; 2016.
[7] Chung D. Cement reinforced with short carbon fibers: a multifunctional material. Compos B Eng 2000;31(6–7):511–26.
[8] Olivito R, Zuccarello F. An experimental study on the tensile strength of steel fiber reinforced concrete. Compos B Eng 2010;41(3):246–55.
[9] Ascione F, Feo L, Maceri F. An experimental investigation on the bearing failure load of glass fibre/epoxy laminates. Compos B Eng 2009;40(3):197–205.
[10] Z¯ıle E, Z¯ıle O. Effect of the fiber geometry on the pullout response of mechanically deformed steel fibers. Cement Concr Res 2013;44:18–24.
[11] Alessi R, Ciambella J, Paolone A. Damage evolution and debonding in hybrid laminates with a cohesive interfacial law. Meccanica 2016:1–13.
[12] Cunha VMCF, Barros JAO, Sena-Cruz JM. Pullout behavior of steel fibers in self-compacting concrete. J Mater Civ Eng 2010;22(1):1–9.
[13] Simões T, Octávio C, Valença J, Costa H, Dias-da Costa D, Júlio E. Influence of concrete strength and steel fibre geometry on the fibre/matrix interface. Compos B Eng 2017;122:156–64.
[14] Isla F, Ruano G, Luccioni B. Analysis of steel fibers pull-out. experimental study, Construction and Building Materials 2015;100:183–93.
[15] Mazaheripour H, Barros JAO, Soltanzadeh F, Sena-Cruz J. Deflection and cracking behavior of sfrscc beams reinforced with hybrid prestressed gfrp and steel reinforcements. Eng Struct 2016;125:546–65.
[16] Alwan JM, Naaman AE, Guerrero P. Effect of mechanical clamping on the pull-out response of hooked steel fibers embedded in cementitious matrices. Concrete Science and Engineering 1999;1(1):15–25.
[17] Khabaz A. Monitoring of impact of hooked ends on mechanical behavior of steel fiber in concrete. Construct Build Mater 2016;113:857–63.
[18] Robins P, Austin S, Jones P. Pull-out behaviour of hooked steel fibres. Mater Struct 2002;35(7):434–42.
[19] Song F. Effect of fibre properties and embedment conditions on fibre pullout behaviour from concrete matrix. In: Muller HS, Haist M, Acosta F, editors. Proceedings of the 9th fib international PhD symposium in civil engineering. Karlsruhe, Germany: KIT Scientific; 2012. p. 597–602.
[20] Fantilli AP, Vallini P. A cohesive interface model for the pullout of inclined steel fibers in cementitious matrixes. J Adv Concr Technol 2007;5(2):247–58.
[21] Laranjeira F, Molins C, Aguado A. Predicting the pullout response of inclined hooked steel fibers. Cement Concr Res 2010;40(10):1471–87.
[22] Mazaheripour H, Barros JAO, Sena-Cruz JM. Tension-stiffening model for FRC reinforced by hybrid FRP and steel bars. Compos B Eng 2016;88:162–81.
[23] Soetens T, Van Gysel A, Matthys S, Taerwe L. A semi-analytical model to predict the pull-out behaviour of inclined hooked-end steel fibres. Construct Build Mater 2013;43:253–65.
[24] Zhan Y, Meschke G. Analytical model for the pullout behavior of straight and hooked-end steel fibers. J Eng Mech 2014;140(12):91–104.
[25] Häßler D, Barros JA. Exploring the possibilities of steel-fiber reinforced self-compacting concrete for the flexural strengthening of masonry structural elements. Int J Architect Herit 2013;7(1):26–53.
[26] Barros JAO, Foster S. Fibres as shear reinforcement in rc beams: an overview on assessment of material properties and design approaches. In: Fibre reinforced concrete: from design to structural application. Joint ACI-fib-RILEM International Workshop; 2018.
[27] Oliveira LF. Design-oriented constitutive model for steel fiber reinforced concrete. PhD Thesis. Universitat Polit`ecnica de Catalunya; 2010.
[28] Valente T. Advanced tools for design and analysis of fiber reinforced concrete structures. PhD Thesis. University of Minho; 2019.
[29] Nonato Da Silva C, Ciambella J, Barros J, Costa I. Analytical bond model for general type of reinforcements of finite embedment length in cracked cement based materials. Int J Solid Struct 2019;167:36–47. https://doi.org/10.1016/j.ijsolstr.2019.02.018.
[30] Cunha VMCF. Steel fibre reinforced self-compacting concrete (from micromechanics to composite behavior). Ph.D. thesis. Escola de Engenharia da Universidade do Minho; 2010.
[31] Häßler D, Barros JAO. Exploring the possibilities of steel-fiber reinforced self-compacting concrete for the flexural strengthening of masonry structural elements. Int J Architect Herit 2013;7(1):26–53.
[32] Htut TNS, Foster SJ. Unified model for mixed mode fracture of steel fiber reinforced concrete. In: Proc. Of fracture mechanics of concrete and concrete structures–high performance, fiber reinforced concrete, special loadings and structural applications; 2010. p. 23–8.
[33] Barros JAO, Varma RK, Sena-Cruz JM, Azevedo AFM. Near surface mounted cfrp strips for the flexural strengthening of rc columns: experimental and numerical research. Eng Struct 2008;30(12):3412–25.
[34] Marti P, Pfyl T, Sigrist V, Ulaga T. Harmonized test procedures for steel fiber-reinforced concrete. Materials Journal 1999;96(6):676–85.
[35] En14651. Test method for metallic fibre concrete. measuring the flexural tensile strength (limit of proportionality (lop), residual), EN 14651 (2005). Brussels: CEN; 2005. + A1 (2007).
[36] Finazzi S, Paegle I, Fischer G, Minelli F. Influence of bending test configuration on cracking behavior of frc. In: 3rd all-Russia (international) conference on concrete and reinforced concrete; 2014. p. 196–205.
[37] Berrocal CG, Löfgren I, Lundgren K, Görander N, Halldén C. Characterisation of bending cracks in r/frc using image analysis. Cement Concr Res 2016;90:104–16.
[38] Salehian H, Barros JAO. Assessment of the performance of steel fibre reinforced self-compacting concrete in elevated slabs. Cement Concr Compos 2015;55:268–80.